1

Introduction to the Theory and Advantages of Low Voltage Electron Microscopy

David C. Bell[1] and Natasha Erdman[2]

[1]*School of Engineering and Applied Sciences, Harvard University, USA*
[2]*JEOL USA Inc., USA*

1.1 INTRODUCTION

The fundamental aspects of electron microscopy all relate directly to the physics of the interactions between the electron beam and sample. These interactions have been studied extensively since the discovery of the electron by J.J. Thompson in 1897. Energetic electrons are described as ''ionizing radiation''—the general term used to describe radiation that is able to ionize or remove the tightly bound inner shell electrons from a material. This is obviously an advantage for electron microscopy in that it produces a wide range of secondary signals such as secondary electrons and X-rays, but is also a disadvantage from the perspective that the sample is ''ionized'' by the electron beam and possibly structurally damaged, which depending on the accelerating voltage happens in a number of different ways. The advantages of using a lower accelerating voltage for the electron beam are that the energy is reduced and hence the momentum that *can* be transferred to sample from the electron is also reduced. This, however, has the unwanted effect of reducing the possible emitted signal; although, with recent improvements in detectors,

Low Voltage Electron Microscopy: Principles and Applications, First Edition.
Edited by David C. Bell and Natasha Erdman.

cameras and the use of aberration correctors, the signal to noise and the resolution to produce a final image can not only be maintained but are actually improved.

This chapter will detail the basic theory of electron beam interactions and how it relates to electron microscopy at low voltage. There are, however, distinct differences between the important considerations for low voltage SEM imaging as compared to TEM imaging and these will be detailed in the text.

1.2 HISTORICAL PERSPECTIVE

The early steps in the development of the electron microscope in the 1930s and 1940s by different research groups led ultimately to the development of two distinct groups of instruments: the scanning electron microscope (SEM) and the transmission (or scanning transmission) electron microscope (TEM and STEM). The early microscope designs by Knoll and by Ruska (1933) showed transmission electron images of solid surfaces at 10–16X magnification, which was improved upon by introduction of replica sample preparation technique for TEM observation (Mahl, 1940). As a continuation of his work with Ruska, M. Knoll had designed an electron beam scanner in 1935 (Knoll, 1935) to study targets for the TV camera tubes; this was in essence a predecessor to an SEM, with accelerating voltage up to 4 kV. In 1936 through his contract with the company Siemens, Manfred von Ardenne began development of a scanning transmission electron microscope, mainly to avoid detrimental effects of chromatic aberration during observation of thick specimens in TEM. The microscope built by von Ardenne had a probe size of 4 nm (von Ardenne, 1937; von Ardenne 1938). The work by von Ardenne, though interrupted by the events of World War II, nonetheless established a theoretical and design background for future SEM and STEM development, particularly regarding understanding of beam/specimen interactions, effect of accelerating voltage on resolution, as well as detector design and positioning within the microscope (von Ardenne, 1985).

From 1938 to 1942, V. Zworykin at RCA headed parallel SEM and TEM development projects that resulted in an SEM instrument with accelerating voltage of 800V (Zworykin *et al.*, 1942). However, poor vacuum in the system significantly impacted the resulting micrographs, and the quality of the recorded images was disappointing with mostly topographic contrast and no meaningful compositional information. These results prompted RCA to discontinue the SEM project

and concentrate on the development of the TEM instrument, and led to the development of several commercial instruments. Nonetheless, the work on SEM instrument development continued in Cambridge in early 1950s (McMullan, 1952; McMullan, 2004). R.F.M. Thornley successfully developed the first low voltage SEM (Thornley, 1960) in Oatley's lab at Cambridge University in the early 1960s. By improving upon the existing SEM2 design (Wells, 1957), he was able to obtain 200 nm probe at 1 kV. Prior to that experiment, the SEM was always operated at higher voltages (greater than 6 kV) that allowed only observation of conductive specimens. Thornley's work showed that a surface of alumina ceramic could be imaged at 1.5 kV negating charging artifacts (Thornley, 1960); moreover, he recognized the importance of low voltage in reducing the charge build up that had caused issues in non-conductive samples.

Over the years, significant improvements in electronics, vacuum and electron column design, as well as detector technology have improved SEM instrument performance to the level where the resolution at 1 kV is on the order of 1–2 nm for high-end field emission systems (see Chapter 2). The recent developments in aberration correction and addition of monochromators to TEM and STEM instruments have further improved their performance for both high and low accelerating voltage applications (see Chapters 6–8).

1.3 BEAM INTERACTION WITH SPECIMEN—ELASTIC AND INELASTIC SCATTERING

Interaction of a primary electron beam with specimen can generate several different signals (Figure 1.1)—secondary and backscatter electrons, transmitted electrons (if the specimen is sufficiently thin), Auger electrons, characteristic X-rays and photons.

The basic elastic and inelastic scattering processes and electron excitation in materials have a direct influence on the electron range and depth of ionization distribution as well as secondary and backscatter electron emission and the observed contrast in all types of electron microscopes. Particle model of elastic and inelastic scattering processes (based on Bohr atom model) is shown in Figure 1.2(a), while Figure 1.2(b) displays band structure with inelastic processes as well as Auger and X-ray emissions, with respect to different energy levels. Multiple elastic scattering events produce electron backscattering; additional multiple inelastic scattering processes lead to eventual energy loss along the electron trajectories deeper within the material that result in the electrons

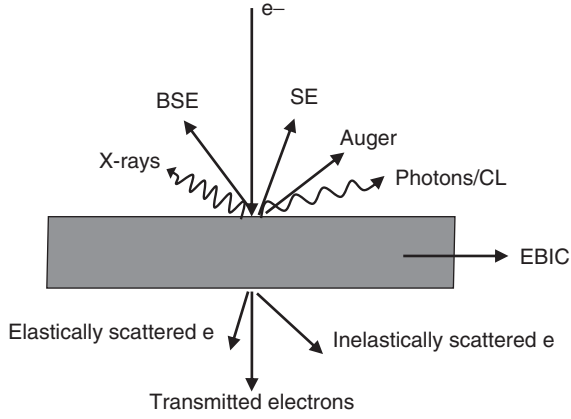

Figure 1.1 Overview of the signals generated when an electron beam interacts with a (relatively) thin specimen. In the case of a thick specimen there are no transmitted electrons and the signal gets absorbed within the material.

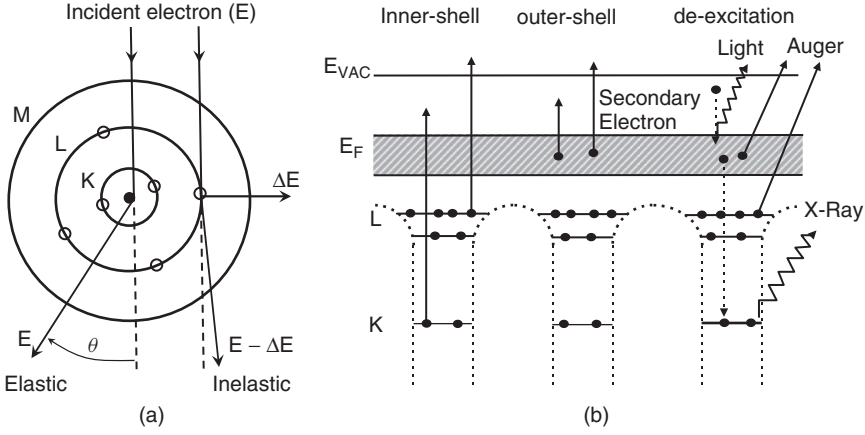

Figure 1.2 (a) Schematic of elastic and inelastic scattering due to the interaction of electron beam of energy E with an atom. (b) Diagram of inelastic excitations, X-ray, photon and Auger emissions with respect to different energy levels.

slowing down and eventually coming to rest. Inelastic scattering is also responsible for the generation of secondary electron signal, Auger electrons, X-rays, electron–hole pairs (semiconductors and insulators), cathodoluminescence and phonon and plasmon production. At lower accelerating voltages, the number of inelastic scattering events decreases;

for example, in Si K-shell ionization is no longer possible if accelerating voltage is below 1.84 kV, an effect known as the Duane-Hunt limit.

Understanding of the elastic and inelastic scattering processes can additionally serve as a basis for modeling of beam/specimen interactions (particularly for SEM imaging and analysis) via Monte–Carlo simulations to investigate electron trajectories in materials and calculate theoretical secondary and backscatter electron spatial distributions based on the specimen position under the beam (angle), accelerating voltage and the material type. Several different programs are available for these types of calculations; more specifically Casino (Drouin *et al.*, 2007; also http://www.gel.usherbrooke.ca/casino/index.html) has been written particularly with a focus on low voltage imaging and analysis.

The quantum mechanical properties of electron are such that the electron has a wavelength defined by de Broglie relationship:

$$\lambda = \frac{h}{p} = \frac{h}{\sqrt{2m_0 E}} \tag{1.1}$$

where h is the Planck constant, m_0 is the rest mass of the electron and E the accelerating voltage. However, since electrons in the electron microscope are moving at high speeds defined by the accelerating voltage of the electron gun this equation needs to be rewritten be become the relativistic version (where E_0 is the rest energy):

$$\lambda = \frac{hc}{\sqrt{2EE_0 + E^2}} \tag{1.2}$$

This means that for a 200 kV electron we have a wavelength of 2.5 pm, but for a 40 kV electron the wavelength becomes nearly three times as large at 6 pm. If we plot wavelength as a function of accelerating voltage, we see that the wavelength increases exponentially as the accelerating voltage decreases below about 20 kV (Figure 1.3). For an SEM operating at 1 kV the wavelength becomes 39 pm, still a small value but a significantly larger wavelength as compared to, for example, 40 kV. The limiting factor for resolution of electron microscope is ultimately the electron wavelength; moreover, the actual working resolution of electron microscopes is directly limited by the lens aberrations present, as detailed later in this chapter. As Figure 1.1 shows, there is a variety of different possible signals generated by the interaction of primary beam with the specimen and to start with we separate these processes based on the differences in the scattering cross section between elastic and inelastic scattering.

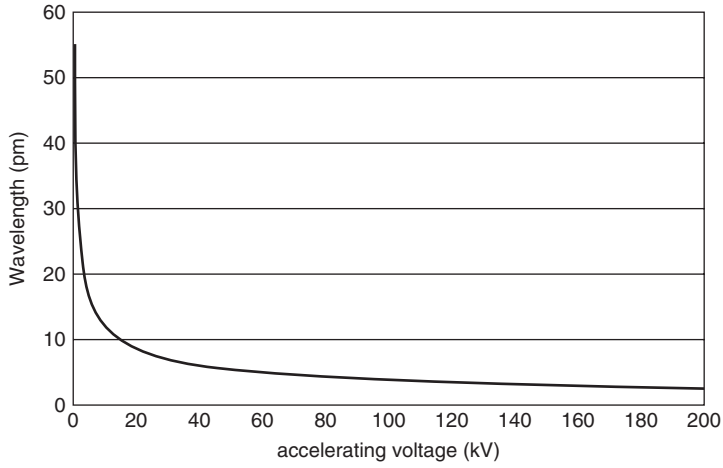

Figure 1.3 Dependence of electron wavelength on the accelerating voltage.

1.3.1 *The Scattering Cross Section*

The probability of an incident electron being scattered by a given atom per unit solid angle Ω is represented by the differential scattering cross section $d\sigma/d\Omega$ that is a function of the scattering angle θ (Figure 1.4). Interaction of the primary beam electrons with the attractive nucleus

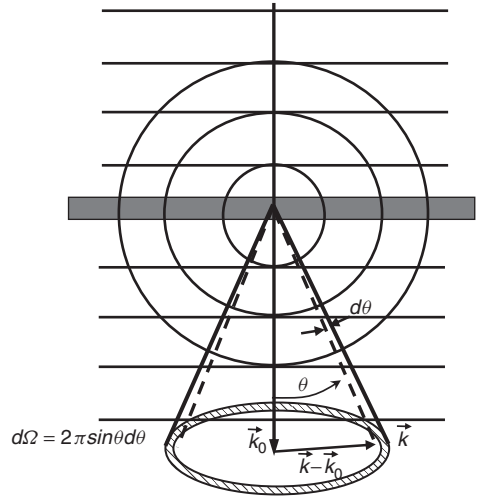

Figure 1.4 Electron scattering as a function of scattering angle θ. Superposition of an incident plane wave with amplitude $\psi = \psi_0 \exp(2\pi i k_0 z)$ and a spherical scattered wave with amplitude $\psi_{sc} = \psi_0 f(\theta) \exp(2\pi i k_0 r)/r$.

Coulomb potential results in elastic scattering processes, with change in a primary electron beam trajectories through angle θ, but negligible energy loss (on the order of meV). For elastic scattering, the cross section is given by:

$$\frac{d\sigma}{d\Omega} = |f(\theta)|^2 \tag{1.3}$$

where f is the scattering factor, which is a function of the scattering angle θ. Assuming a single scattering within each atom (the first Born approximation), scattering factor is proportional to the tree dimensional Fourier transform of the atomic potential *V(r)*. The elastic scattering cross section can also be expressed as a function of an elastic scattering factor *F(q)*:

$$\frac{d\sigma}{d\Omega} = \frac{4}{a_0^2 q^4} |F(q)|^2 = \frac{4\gamma^2}{a_0^2 q^4} \left|Z - f_x(q)\right|^2 \tag{1.4}$$

where $f_x(q)$ is the atomic scattering factor of an incident photon and equals the Fourier transform of the electron density within the atom; $a_0 = 4\pi\varepsilon_0\hbar^2/m_0e^2 = 0.529 \times 10^{-10}$ m is the Bohr radius, $\gamma = (1-v^2/c^2)^{-1/2}$ is a relativistic factor and $q = 2k_0\sin(\theta/2)$ is the scattering vector. The incident electrons are scattered by the entire electrostatic field of the atom (as opposed to X-rays that interact only with the atomic electrons), hence the inclusion of the atomic number (or nuclear charge) Z in Equation (1.4).

The relatively simple Rutherford scattering model (Rutherford, 1911) has been widely used in the past to describe elastic scattering of charged particles based on the unscreened electrostatic field of a nucleus. Setting the electronic term, $f_x(q)$, in Equation (1.4) to zero, the differential cross section becomes:

$$\frac{d\sigma}{d\Omega} = \frac{4}{a_0^2 q^4} Z^2\gamma^2 \tag{1.5}$$

The above equation is a reasonable approximation for light elements at large scattering angles (and has been often employed for modeling of high kV SEM imaging); however, at small scattering angles the equation breaks down, mainly due to the fact that the nuclear screening is not taken into account.

The nuclear screening can be incorporated via an expression for nuclear potential attenuated exponentially as a function of distance from the nucleus (r):

$$V(r) = \left(\frac{Ze}{4\pi\varepsilon_0 r}\right)\exp\left(-\frac{r}{r_0}\right) \tag{1.6}$$

where r_0 is the screening radius. The elastic scattering cross section then becomes:

$$\frac{d\sigma}{d\Omega} = \frac{4\gamma}{a_0^2}\left(\frac{Z}{q^4 + r_0^2}\right)^2 \approx \frac{4\gamma^2 Z^2}{a_0^2 k_0^4}\frac{1}{\left(\theta^2 + \theta_0^2\right)^2} \tag{1.7}$$

where $\theta_0 = (k_0 r_0)^{-1}$ and $r_0 = a_0 Z^{-1/3}$ (Lenz, 1954). The model in Equation (1.7) provides a quick estimate of the angular dependence of scattering; however, there are more sophisticated methods for calculating cross sections that take into account relativistic effects (for example Mott scattering cross section), and are particularly relevant at low incident energies.

A more accurate treatment of the elastic scattering cross section is achieved by taking into account relativistic quantum mechanics based on the Dirac equation. For example, Mott scattering cross-section (Mott, 1932; Mott and Massey, 1949; Reimer, 1993) incorporates the effect of spin-orbit coupling of electrons and thus differs from Rutherford scattering. Mott cross-section is especially applicable when describing beam-specimen interactions in the case of low voltage SEM observation. Mott cross-section is a quite complex function of primary electron energy, atomic number and scattering angle and several empirical models based on tabulated values have emerged and are being currently used in various beam/specimen interactions simulation programs (Czyzewski *et al*., 1990; Gauvin and Drouin, 1993; Browning *et al*., 1995; Hovington *et al*., 1997).

Inelastic scattering is typically described as scattering events that result in energy loss of ΔE for the primary beam electrons through energy transfer to the atoms in the sample through interaction with either outer or inner shell atomic electrons; however, inelastic scattering does not significantly alter the electron trajectory.

The differential cross section for inelastic scattering can be written as (Reimer and Kohl, 2008):

$$\frac{d\sigma_i}{d\Omega} = \frac{4\gamma^2 Z}{a_0^2 q^4}\left(1 - \frac{1}{\left[1 + (qr_0)^2\right]^2}\right) \tag{1.8}$$

in which the scattering vector q is given by:

$$q^2 = k_0^2\left(\theta^2 + \overline{\theta}_E^2\right) \tag{1.9}$$

where $k_0 = 2\pi/\lambda$ is the magnitude of the incident electron wave vector, θ is the scattering angle, $\overline{\theta}_E = \overline{E}/\gamma m_0 v^2$ is the angle associated with the mean energy loss of $\overline{E}$. The above two expressions can be combined to give the expression for inelastic scattering cross section as a function of the scattering angle (Colliex and Mory, 1984):

$$\frac{d\sigma_i}{d\Omega} = \frac{4\gamma^2 Z}{a_0^2 k_0^4}\frac{1}{\left(\theta^2 + \overline{\theta}_E^2\right)^2}\left\{1 - \left[1 + \frac{\overline{\theta}_E^2}{\theta_0^2} + \frac{\theta^2}{\theta_0^2}\right]^{-2}\right\} \tag{1.10}$$

Figure 1.5 illustrates angular distribution of elastic and inelastic scattering cross sections calculated in carbon at an accelerating voltage of 100 kV showing how the scattering cross section decreases rapidly from zero degrees, interestingly of note is how the inelastic scattering

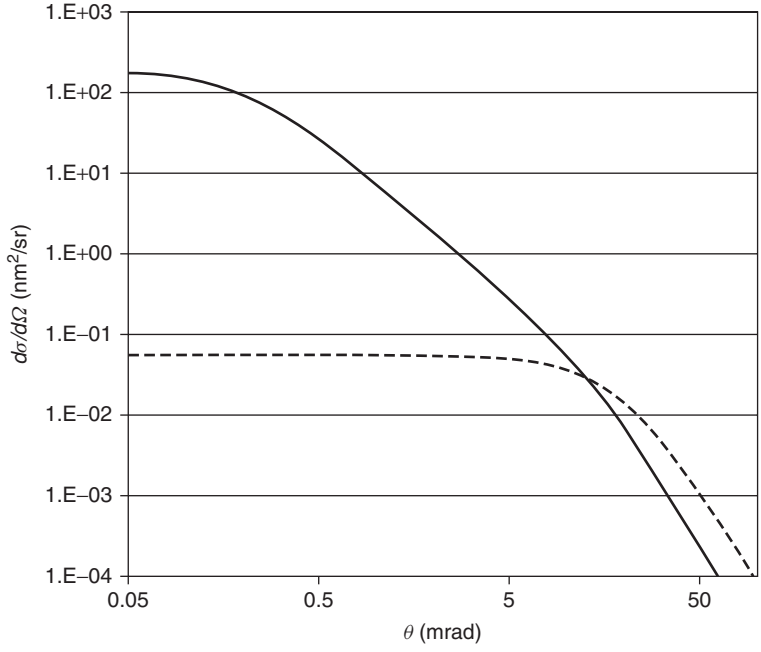

Figure 1.5 Angular dependence of elastic (dashed line) and inelastic (solid line) cross sections for carbon at accelerating voltage of 100 kV.

starts higher than elastic and then drops off more rapidly than the elastic. For more detailed discussion and analysis of differential cross sections see for example Egerton (2011) and Reimer and Kohl (2008).

1.3.2 *Effects of Specimen Damage*

Although elastic and inelastic scattering processes are essential for imaging and spectroscopy in electron microscope, they are also responsible for the electron beam induced specimen damage and alteration. The two most common damage mechanisms are termed radiolysis and knock-on damage.

Knock-on damage occurs when the incident electron energy is higher than the atomic sputtering threshold energy (Mott, 1932; Hobbs, 1979), thus inducing either an atom removal from its site or sputtering from the surface. The maximum energy that can be transferred to an atom during a collision is:

$$E_{\max} = \frac{2E(E + 2m_0c^2)}{M_0c^2} \tag{1.11}$$

where E in the incident electron energy, M_0 is the mass of the atom, and m_0c^2 is the rest energy of the electron. Equation (1.11) describes the threshold energy (E_{th}) needed for incident electrons to displace or sputter atoms.

Radiolysis damage is induced by converting the exciton energy generated by incident beam interaction with specimen into momentum and thus creating atomic displacements in the analyzed material (Hobbs and Pascucci, 1980; Pascucci, 1983). In order for radiolysis to occur the exciton energy should be larger than the energy needed for atomic displacement, and the exciton relaxation time should be sufficiently long ($\geq$1 ps) such that the bonding instabilities can be induced by mechanical relaxation of the atoms. Radiolysis processes are common in materials like organic compounds, silicates, halides and ice (Hobbs, 1979).

Some recent experimental observations and theoretical predictions suggest that below incident energies of 70 kV the damage is mainly radiolitic; whereas at incident energies above 200 kV the knock-on damage and material sputtering will be dominant (Ugurlu *et al*., 2011). Therefore, TEM and STEM imaging at low voltages should substantially reduce knock-on damage.

1.4 INSTRUMENT CONFIGURATION

1.4.1 *Scanning Electron Microscope*

The scanning electron microscope (SEM) operates by rastering a fine electron probe (few nm in size) over a region of the specimen. Typical scanning electron microscope configuration is shown in Figure 1.6(a). Contemporary SEM instruments usually operate between few tens of volts and 30 kV, and are traditionally used for examination of bulk materials, though very thin specimens can be examined in transmission mode as well. The spatial resolution of the instrument is characterized by the electron probe diameter that can be achieved with the combination of electron source size and the lens configuration; however, the beam/specimen interaction volume further limits the instrument resolution. The instrument can collect (depending on the detector configuration) secondary, backscatter and transmitted electron signals. Moreover, signals like X-ray emission (EDS and WDS), cathodoluminescence (CL), electron backscatter diffraction (EBSD) and electron beam induced current (EBIC) can be detected.

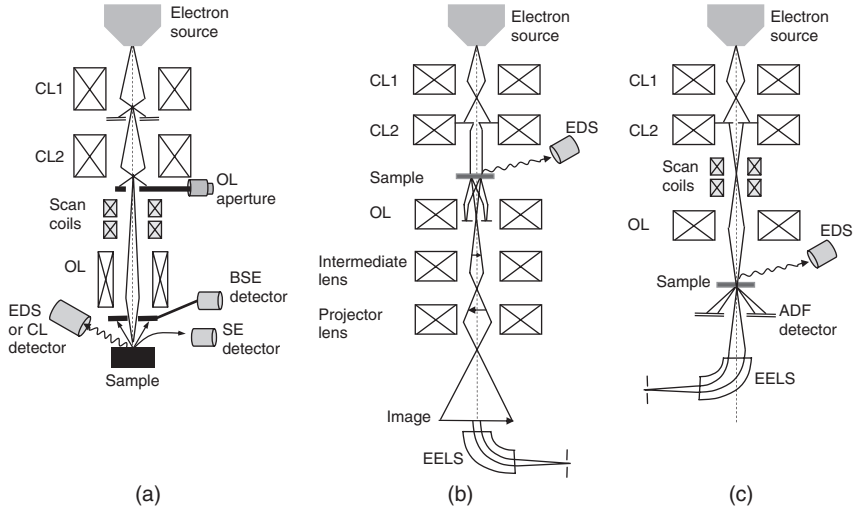

Figure 1.6 Simplified schematic cross-sections of an (a) SEM, (b) TEM and (c) STEM instrument.

1.4.2 *Transmission Electron Microscope*

In transmission electron microscope (TEM) a very thin specimen (less than 100 nm thick) is irradiated by a beam of high-energy electrons (between few tens of kV up to 1 MeV). A schematic of a traditional TEM configuration is presented in Figure 1.6(b). The TEM allows examination of specimens with an order of magnitude higher resolution than an SEM; the resolution of a non-aberration corrected TEM with field emission source is ~1.2 Å, whereas contemporary aberration corrected systems have been shown improve resolution down to 0.5 Å. Crystallographic information can be obtained in TEM using either selected area or convergent beam diffraction modes; elemental characterization can be obtained by utilizing either energy dispersive spectroscopy (EDS) or electron energy loss spectroscopy (EELS).

1.4.3 *Scanning Transmission Electron Microscope*

A dedicated scanning transmission electron microscope (STEM) utilizes a field emission gun that generates a probe size on the order of 1 Å that is rastered across an electron transparent specimen (Figure 1.6c). The instrument is typically operated at 80–300 kV accelerating voltage. The signal detection relies on the angular distribution of the scattered electrons with the ability to detect both electrons that are elastically scattered through high angles (high annular dark field, HAADF) and electrons that are inelastically scattered through small angles. HAADF signal contrast is indicative of the atomic number distribution (also called Z-contrast). The addition of EDS and EELS spectrometers further enhances the microscope, with the ability to perform atomic column specific analysis on the current aberration corrected instruments (e.g., Muller *et al*., 2008; Botton *et al*., 2010).

1.5 INFLUENCE OF ELECTRON OPTICS ABERRATIONS AT LOW VOLTAGES

The electron optical system performance is most often characterized by the minimum size of the electron probe that can be produced and the corresponding beam current in that probe size. However, the existing lens aberrations in the electron optical system assure that there is a limit to how small the spot of the electron beam can be focused into and the probe current that can be delivered in that spot. From the brightness equation:

$$\beta = \frac{I_b}{\pi.d_g^2/4} \quad \frac{1}{\pi.\alpha^2} = \frac{4I_b}{\pi^2.\alpha^2.d_g^2} \tag{1.12}$$

it is clear, that the amount of current (I_b) for a given Gaussian spot size d_g will depend on the square of the convergence angle (α^2), while the brightness (β) is constant.

The lens aberrations are often classified by their order (Hawkes and Kasper, 1985)—defocus (first order), chromatic aberration (second order) and spherical aberration (third order). There are also first and third order astigmatism as well as axial coma (second order), which can be corrected by a more precise mechanical and electromagnetic column alignment, as well as use of smaller beam aperture sizes.

1.5.1 *Spherical Aberration*

Figure 1.7(a) shows a schematic representation of cause of spherical aberration in a round lens. The parallel rays incident on the electron lens are focused at different planes based on their angle of incidence and the refractive index of the lens; the rays traveling at high angles are focused

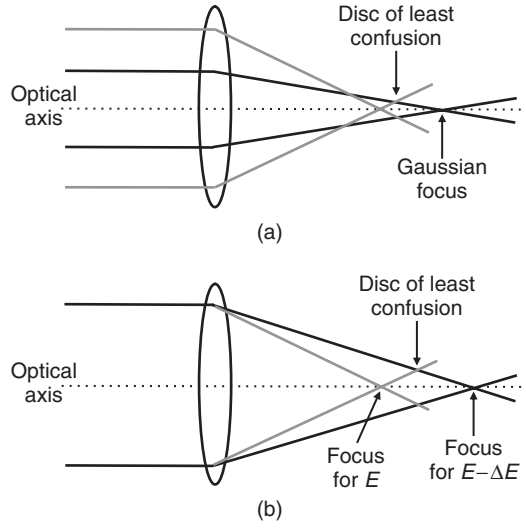

Figure 1.7 Schematic representation of (a) spherical and (b) chromatic aberration effects.

closer to the lens than the ones traveling at small angles. The desired focused spot thus becomes a disc stretched along the optic axis between the Gaussian focus and the lens, and called the disc of least confusion. The diameter of this disk (spot size) is (Cosslett, 1972):

$$d_s = 0.5 \cdot C_s \cdot \alpha^3 \tag{1.13}$$

where α is the convergence angle and Cs is spherical aberration coefficient. The minimum spot size (taking into account spherical aberration) therefore is proportional to α^3, while the current that can be delivered in the spot is proportional to α^2. These relationships force the user then to potentially sacrifice spot size for analytical performance or vice versa. In SEM spherical aberration can be minimized by working at very short working distances (in semi-in-lens systems Cs values can be brought down to 1–2 mm; for in-lens systems the Cs value can be as small as 50 μm - Joy, 2008) or by employing an aberration corrector (see Chapter 2). In TEM/STEM the spherical aberration effects are typically corrected via incorporation of higher order aberration corrector (Haider, 1995; Rose, 2009).

1.5.2 *Effect of Chromatic Aberration*

Chromatic aberration comes into play as a consequence of an energy spread in the electron beam produced by the electron source, resulting in longer focal distances for rays with higher energies and shorter distances for lower energies (Figure 1.7b). The effect of chromatic aberration on the resulting spot size (disc of least confusion) can be expressed as:

$$d_c = C_c \cdot \alpha \cdot \frac{\Delta E}{E_0} \tag{1.14}$$

where Cc is chromatic aberration coefficient, $\Delta E/E_0$ is the energy spread with respect to the primary beam energy, and α is the convergence angle. The spot size dependence on *1/E* suggests stronger effect of chromatic aberration as accelerating voltage is lowered, and becomes the dominant effect below 2 kV in SEM and 40 kV in TEM/STEM (Bell *et al*., 2012). The effect of chromatic aberration can be minimized by employing a Cc corrector or by using a monochromator. Chapter 3 discusses incorporation of monochromator in modern SEM; Chapter 6 discusses the TEM monochromator.

1.5.3 *The Diffraction Limit*

The Airy disc is formed by the interference between the electrons traveling along the optical axis and the electrons scattered by the lens. The width of the beam d_d is a distance between the first-order zeroes in the Airy disc and is given by:

$$d_d = 0.6\frac{\lambda}{a} \tag{1.15}$$

and the deBroglie wavelength λ (in nm) for low energy electrons can be defined as:

$$\lambda = \frac{1.226}{\sqrt{E_0}} \tag{1.16}$$

where E_0 is the beam energy in eV. As the electron energy is lowered, the wavelength is increased, which then requires increase in the convergence angle to maintain negligible effect of diffraction effects on ultimate probe size. The schematic representation of the diffraction error is shown in Figure 1.8. Of course, other lens aberrations, such as coma, can be avoided by performing a coma free or on-axis alignment or by using small beam apertures and/or aberration corrected electron optics.

1.5.4 *Optimizing Spot Size for SEM and STEM*

The effects of all the aberration on the ultimate resolution that can be achieved in the electron microscope can be summed up as follows:

$$d_{eff}^2 = \left(0.6\frac{\lambda}{\alpha}\right)^2 + (0.5\cdot C_s\alpha^3)^2 + \left(C_c\cdot\alpha\frac{\Delta E}{E_0}\right)^2 + d_g^2 \tag{1.17}$$

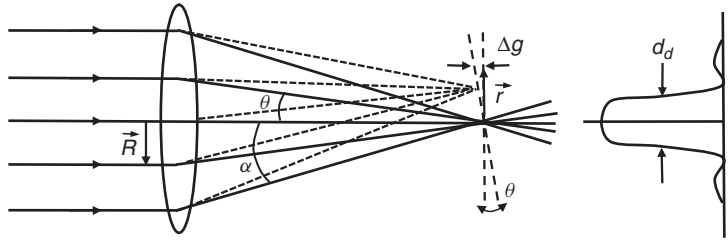

Figure 1.8 Schematic representation of the diffraction error.

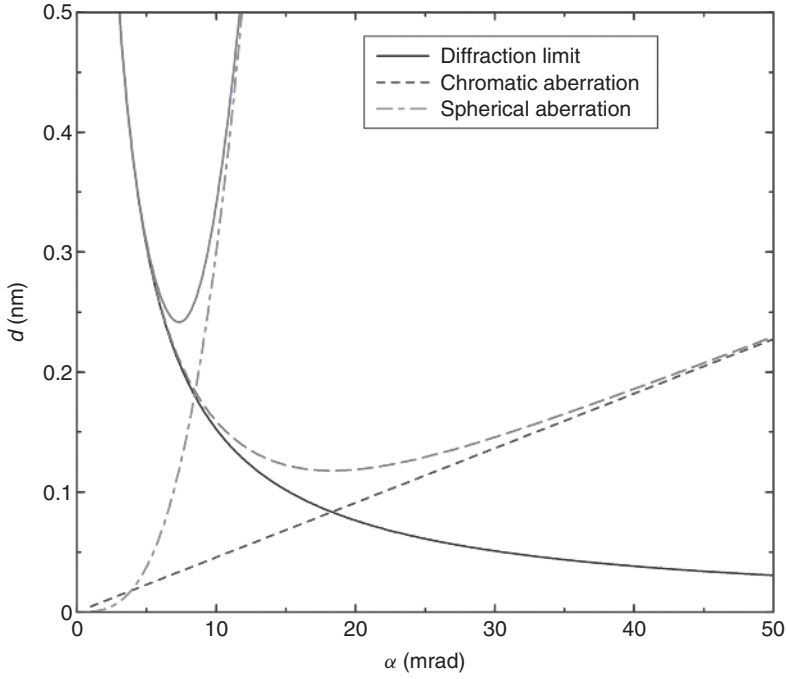

Figure 1.9 Effect of instrument aberrations on the probe size in electron microscope as a function of convergence angle α. The plot is for 200 kV, $\Delta E = 0.7$ eV, Cs = 1.2 mm, Cc = 1.3 mm.

The equation depicts a complex relationship between the effective probe size d_{eff}, the convergence angle and the accelerating voltage. The equation holds true for both scanning and transmission electron optical systems.

Figure 1.9 shows as an example a typical plot of spot size as a function of convergence angle for the Zeiss Libra 200 MC TEM. The plot indicates the limiting effects of instrument aberrations on the probe size in electron microscope as a function of convergence angle α for accelerating voltage of 200 kV, energy spread of $\Delta E = 0.7$ eV, and aberration coefficients of $Cs = 1.2$ mm and $Cc = 1.3$ mm .

1.6 SEM IMAGING AT LOW VOLTAGES

When scanning electron beam impacts a specimen in SEM, several different signals can be generated according to Figure 1.1. The individual signals are associated with a specific volume from which they are produced, and the range of the signals and their spatial distribution depend

on the accelerating voltage as well as the type of material. Figure 1.10 shows a schematic diagram of the interaction volume of the primary electron beam with a specimen in SEM as well as the signal range. The energy spectrum in Figure 1.11 shows a representation of distribution of backscatter and secondary signals collected in the SEM. The spectrum shows a peak of elastically (low-loss) reflected BSEs, plasmon loss peaks

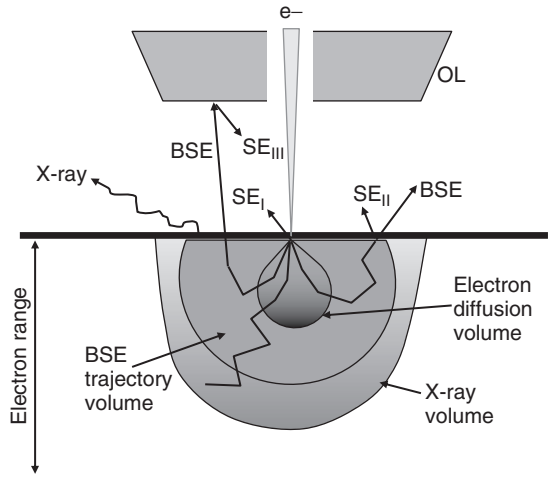

Figure 1.10 Beam/specimen interaction in SEM showing the resulting electron trajectories, generated signals and respective interaction volumes.

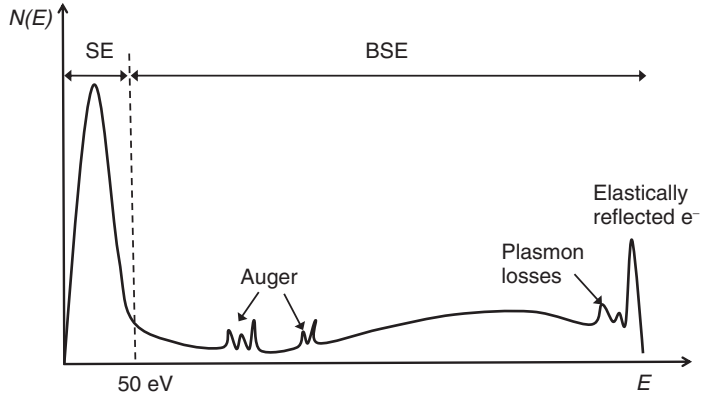

Figure 1.11 Energy spectrum N(E) (arbitrary units) of electron emission, showing secondary (SE), backscatter (BSE), Auger electrons regions.

and inner-shell ionization edges (inelastic scattering contribution), as well as Auger electrons (100–2000 eV) that can be generated from very thin surface layers. Next, we will discuss the basic concepts in SEM signal generation and detection, especially as they pertain to low voltage imaging. For further reading, there are various texts on SEM imaging and beam/solid interactions (e.g., Dekker, 1958; Seiler, 1983; Reimer, 1993; Joy and Joy, 1996; Joy, 1995; Goldstein *et al*., 2003)

1.6.1 *Primary Contrast Signals and their Detection in SEM*

At lower accelerating voltages in SEM the beam/specimen interaction volume is substantially reduced as compared to high voltage operation, since the mean free path and penetration depth of the beam electrons are smaller (lower energy electrons loose energy faster). Moreover, the interaction volume is also dependent on the atomic number: the mean free path is longer in low Z materials versus high Z materials. High Z materials produce stronger Coulomb interactions (higher degree of elastic scattering), thus reducing the overall size of the interaction volume. These concepts are demonstrated in Figure 1.12 for carbon and gold, comparing beam/specimen interactions at 0.1 kV (assumed spot size is 5 nm) and 5 kV (spot size 2.5 nm). The image at 5 kV shows the familiar contrast where gold grains are white and the carbon support is black; however, at 0.1 kV the contrast is reversed and the gold grains have the same contrast as carbon. This phenomenon is easily explained by comparing beam specimen interactions at 0.1 kV versus 5 kV; at ultra-low voltages the interaction volumes are nearly identical. It becomes therefore apparent, that a priori knowledge of the material being analyzed in SEM is of outmost importance, since the choice of accelerating voltage will govern the understanding of the signals being produced and detected.

1.6.2 *Backscattered Electrons*

Backscattered electron signal is generated by the primary beam electrons that have undergone multiple elastic and inelastic collisions with specimen atoms and are reflected back through the specimen surface. The backscattering coefficient η is defined as the fraction of the primary electrons leaving the specimen with energies above 50 eV. The backscattering coefficient increases monotonically with incident electron angle and increasing atomic number Z, for accelerating energies

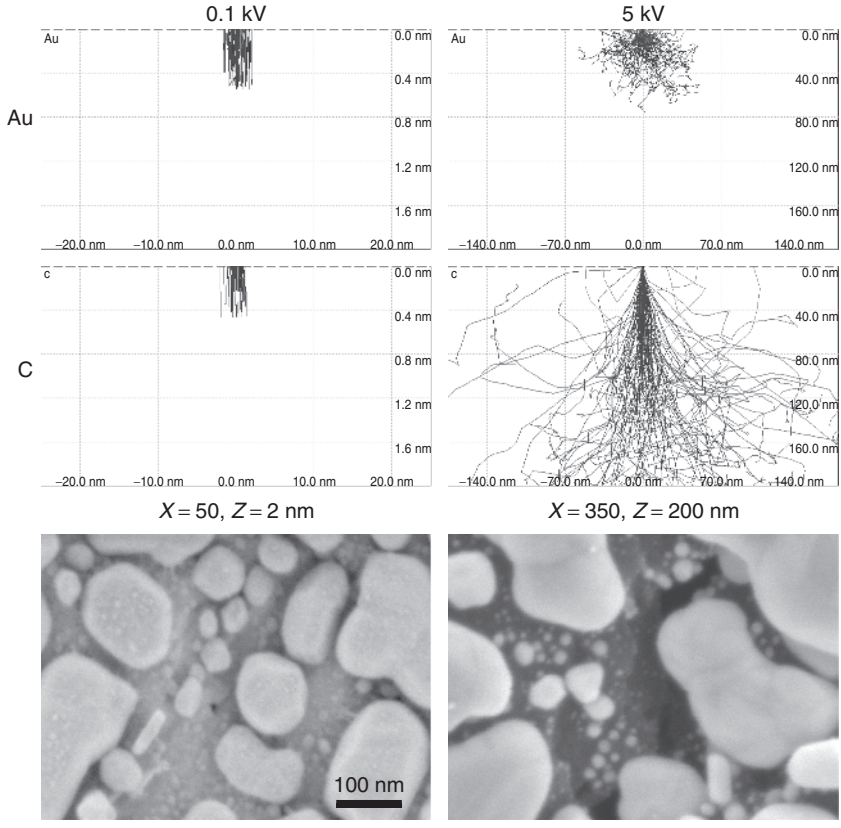

Figure 1.12 Monte Carlo simulation (CASINO®) of electron trajectories in Au and C as a function of accelerating voltage (top). Corresponding images are shown at the bottom.

above 5 kV, Figure 1.13(a) (Darlington, 1975; Drescher, *et al.*, 1970; Goldstein *et al.*, 2003):

$$\eta(Z,\phi) = 0.89 \cdot \left(\frac{\eta(Z,0)}{0.89}\right)^{\cos\phi} \tag{1.18}$$

$$\eta(Z,0) = -0.0254 + 0.016.Z - 1.86.10^{-4} \cdot Z^2 + 8.3 \cdot 10^{-7} \cdot Z \tag{1.19}$$

where ϕ is the specimen tilt angle. However, the BSE coefficient behavior changes substantially at low voltages, mainly due to the Mott elastic cross-section, as demonstrated in Figure 1.13(b). As a general trend, the plot shows that η increases with decrease in energy for $Z<30$ and decreases for $Z>30$ at low accelerating voltages (less than 5 kV)

(Darlington and Cosslett, 1972; Reimer and Tollkamp, 1980; Kotera *et al*., 1981a; Kotera *et al*., 1981b; Schmid *et al*., 1983). Importantly, the trend of the plot suggests that at low voltages the BSE image contrast can be somewhat complicated and the user should be extremely careful about image interpretation.

An example of this complicated contrast phenomenon is shown in Figure 1.14; a sample of Ni/Pt eutectic with AlN spheres was imaged with a low angle solid-state backscatter detector at 0.5, 2 and 5 kV. Although 5kV image shows distinct contrast differences between Ni and Pt while the lower Z AlN spheres have darker contrast, reducing

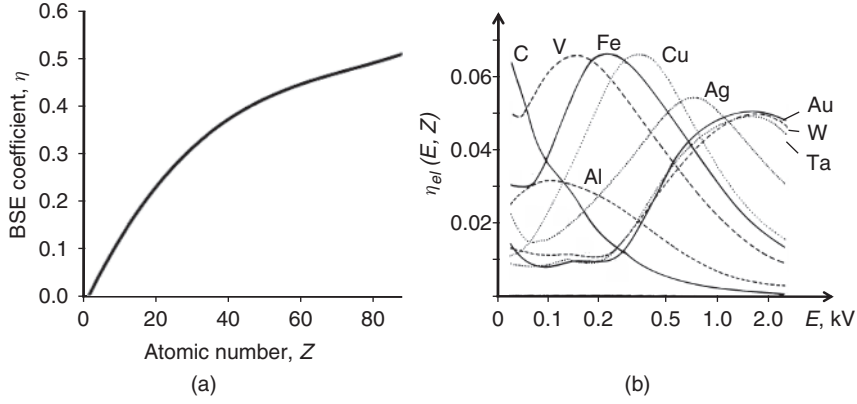

Figure 1.13 (a) Backscatter coefficient as a function of atomic number, *Z*; (b) Elastic backscatter coefficient for different materials as a function of accelerating voltage (after Schmid *et al*., 1983).

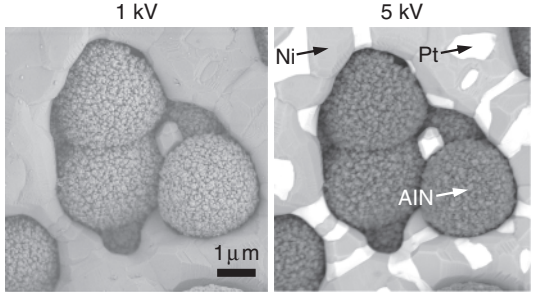

Figure 1.14 An example of BSE contrast reversal upon lowering accelerating voltage. Sample: ceramic eutectic. The images were taken with low angle solid state BSE detector (JEOL USA).

the accelerating voltage down to 0.5 kV essentially eliminates contrast differences between Ni and Pt as well as metals and ceramic components.

1.6.3 *Secondary Electrons*

The SE yield (δ) is defined as the mean number of secondary electrons excited per incident electron. The probability of the secondary electrons escaping from a surface can be given by:

$$p(z) = 0.5\exp\left(\frac{-z}{\lambda}\right) \tag{1.20}$$

where λ is a mean free path (or escape depth) of the electrons propagating to the surface. Seiler (1983) demonstrated that λ is approximately 1 nm in metals and up to 20 nm in insulators. The maximum depth of emission is approximately 5λ. Traditionally, the electrons emitted with energies below 50 eV are considered to be secondary electrons (see Figure 1.11), and their energy spectrum distribution is independent of accelerating voltage (if $E_{acc} > 0.1$ kV). The secondary emission can be characterized by a curve with a peak at approximately 2–5 eV (Figure 1.15a); the peak's general shape is essentially the same for various materials. However, the width of the peak as well as its position vary between different materials and with presence of surface contamination layers; the width of the peak is narrower and its position shifts towards lower energies for insulators as compared to metals (Bouchard and Carette, 1980; Seiler, 1983; Cazaux, 2008). A typical value for δ is $\sim$0.1 for most elements; the value for Au is 0.2 and for C is 0.05. The maximum SE yield can

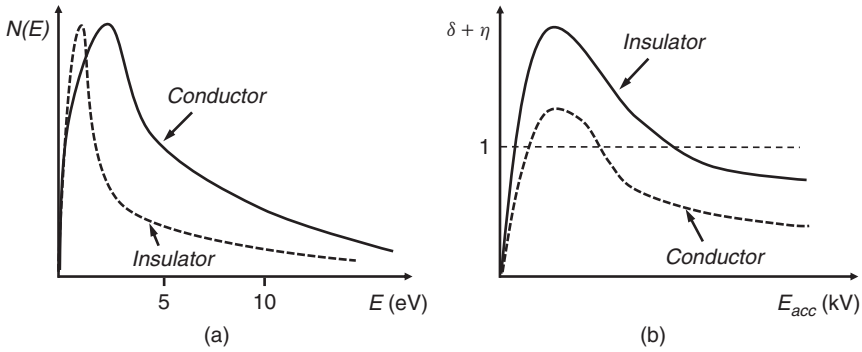

Figure 1.15 (a) Typical energy distribution of SE electrons from conductors and insulators; (b) Total electron yield as a function of primary electron energy.

be achieved when the electron range in the sample is approximately the escape depth of the secondary electrons.

Secondary electrons are further divided into three categories, based on their origin. SE_I electrons are generated within the top 1–10 nm of the specimen, and are the only electrons that contribute to high resolution on the order of electron probe size. SE_{II} electrons are produced by backscattered electrons within the interaction volume on the order of 0.1–1 μm in diameter at high kV, and 5–50 nm at low kV (depending on the material). For high Z materials, SE_{II} signal is approximately 1.5 times larger than SE_I signal; for low Z materials the ratio of SE_{II} to SE_I is approximately 1/5. SE_{III} signal is what is often referred to as "system electrons", originating from BSEs interacting with the parts of the SEM chamber or most likely with the bottom of the objective lens and producing SE signal. In certain semi in-lens systems, conversion to SE_{III} electrons is used to boost the amount of SEs that can be detected by the in-lens detector, especially at low voltages.

Taking into account both secondary and backscattered electron emission, the total electron yield is therefore:

$$\delta = \delta_{SE} + \delta_{BSE} \tag{1.21}$$

Comparison of the total electron yield behavior for metals and insulators is shown in Figure 1.15(b). At high kVs (above 5 kV), δ is below unity; however, as the accelerating voltage is lowered, the total yield increases until it reaches a crossover point E_2 where $\delta = 1$. Further reduction in accelerating voltage leads to a maximum in total yield ($\delta > 1$), and follows by a decrease to another crossover point E_1 where the total yield $\delta = 1$ again. This behavior can be explained by significant increase in SE yield between the two crossover points due to the decrease in interaction volume as a function of accelerating voltage; the shallow interaction volume between E_1 and E_2 results in larger number of electrons within the escape depth of the specimen able to leave the surface as SEs. This phenomenon should be taken into consideration when selecting the imaging conditions for heterogeneous materials; at low accelerating voltages the image may show reversal of contrast based on the choice of voltage with respect to points E_1 and E_2.

The SE yield (similar to backscattered yield) is also dependent on the specimen tilt with respect to the primary beam, and follows a secant law, $\delta(\theta) = \delta_0 \sec(\theta)$. This dependence is demonstrated in Figure 1.16. Similar considerations also come into play when considering sample features like corners, steps or edges, which inevitably increase SE emission.

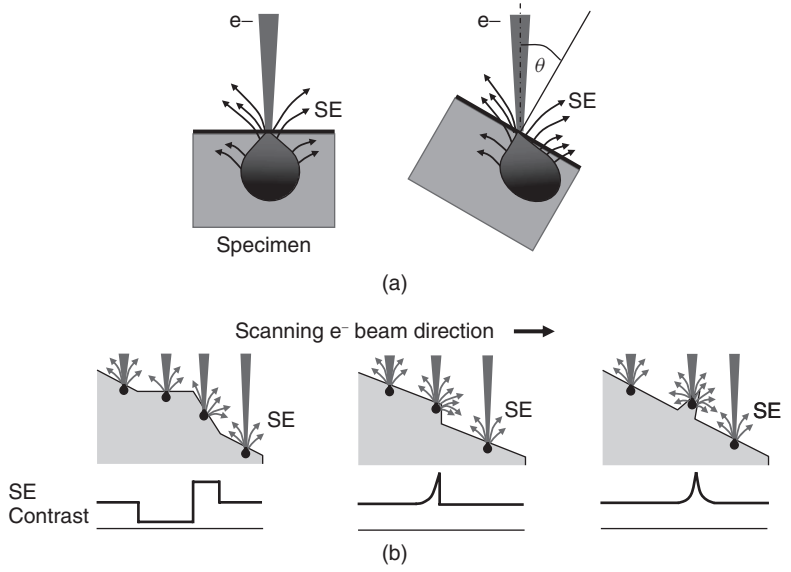

Figure 1.16 (a) Secondary electron yield as a function of tilt angle with respect to the primary beam. (b) Schematic representation of the resulting detected SE contrast (E/T detector) as a function of specimen topography.

1.6.4 *Charge Balance in SEM*

Interaction of primary beam with insulating specimen can produce a surplus or deficit of electrons on the specimen surface that results in the buildup of unstable and inhomogeneous electric fields and leads to charging and inability to image the specimen. If the accelerating voltage is chosen to be equal to E_1 or E_2 crossover energies, the number of incident electrons equals the number of emitted electrons (SE and BSE), thus the net charge is zero. The regions where $E<E_2$ or $E>E_1$ are considered regions of "white" charging; when the accelerating voltage is chosen to be $E_1<E<E_2$ the specimen exhibits "black" charging. Up till recently it was fairly straightforward to image in the region between E_1 and E_2; however, going below E_1 for most materials has been very difficult due to instrument limitations. The new instrument designs that allow imaging down to few tens of volts with fairly high resolution can alleviate these concerns. Figure 1.17 shows an example of pollen grain imaged in the "black" contrast ($E_1<E_{acc}<E_2$) region and ultra-low voltage ($E<E_1$) region with contrast reversal and minimal charging. Additional information regarding crossover energies values for various

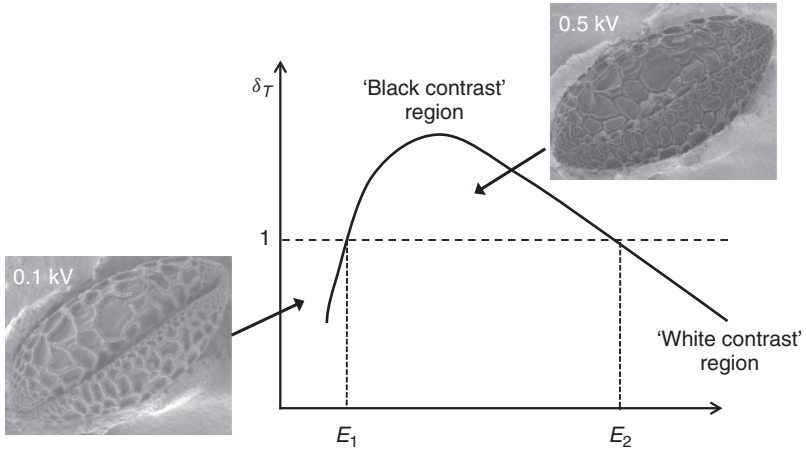

Figure 1.17 Total electron yield as a function of energy, showing with regions of possible contrast reversal. Images of pollen grain at various corresponding voltages shown as insets.

materials can be found in Seiler (1983), Joy and Joy (1996), Goldstein *et al*. (2003).

Low voltage imaging can be particularly useful for charge reduction. However, care should be taken in the case of imaging of rough specimens as well as composites of insulating and conducting materials, since charge dissipation may not be as straightforward because of the complex nature of the electric fields generated on the specimen surface. In addition to lowering the accelerating voltage for charge reduction, the user may consider lowering the probe current as well as changing scan speed to acquire the image (in particular, use line or frame integration). Chapter 2 will discuss the strategies employed in newly designed FE-SEM instruments for charge compensation and imaging of insulating materials.

1.6.5 *SEM Image Contrast*

One of the main advantages of low accelerating voltage SEM is the ability to tap into different types of contrast mechanisms that are only available through changes in electron range, secondary electron yield and backscatter electron coefficients of elements due to low kV operation. The main types of contrast mechanisms that undergo substantial changes as compared to the more traditional high kV observation are listed next:

- Topography
- Material (compositional) contrast
- Crystal orientation or channeling

- Thin film, coating or contamination layer contrast
- Voltage contrast
- Magnetic domain contrast

As was shown previously by Monte-Carlo simulations, there is a substantial difference in interaction volume between SE and BSE signals at higher accelerating voltages; at low kVs these differences are dramatically reduced, which leads to some very interesting reversals of traditionally expected topographic and material contrast as well as added benefits for surface imaging. Further discussion and examples of the contrast mechanisms at low voltages can be found in (Cazaux, 2004; Cazaux, 2008). In Chapters 2 through 4 we will discuss examples of a variety of material and biological specimens imaged and analyzed at low voltages, showing distinct advantages of low kV operation.

1.6.6 *Microanalysis in SEM at Low Voltages*

One of the major benefits of low voltage microanalysis is increased spatial resolution through the reduction of beam/specimen interaction volume; moreover, lower accelerating voltage may allow longer analysis times for beam sensitive specimens. An example of thin section of ore imaged and analyzed at various accelerating voltages is shown in Figure 1.18; there is an obvious benefit to operating at 5 kV versus 15 kV to resolve the fine material composition and microstructure. Microanalysis at lower voltages can determine chemical composition of thin films, nanoparticles, surface layers and light elements (Boyes, 2000; Rowlands *et al*., 2009).

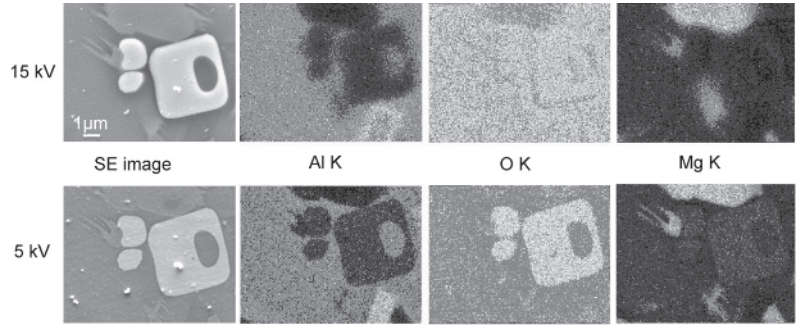

Figure 1.18 Advantage of X-ray microanalysis at low voltages in SEM. WDS maps of polished section of ore from Miake Island. Elemental maps of Al, O and Mg shown alongside corresponding SE images, taken at 15 kV (top) and 5 kV (bottom) (See plate section for coloured version).

As with SEM imaging, the microanalysis techniques (such as EDS, WDS and CL) have focused in the past on the use of high accelerating voltage, mainly due to the requirement for adequate X-ray signal detection without the need to spend hours and even days performing a single analysis. The ability to collect X-ray signal with all the characteristic lines present, thus (hopefully) eliminating all the potential issues associated with element lines overlaps has also driven researchers towards higher accelerating voltages. However, the most important and limiting factor for low voltage microanalysis until recently has been the fact that a relatively large probe size at low accelerating voltage and high beam current necessary for analysis prevented the user from taking advantage of the reduced interaction volume and thus better spatial resolution provided by low kV operation. This paradigm has changed in the recent years with the development of FEG-SEMs that boast nanometer size resolution at 1 kV, and maintain relatively small probe size even when beam current is increased into several nA range necessary for microanalysis (see Chapter 2). The new advances with the EDS detector design and analysis software improvements (e.g., Kenik *et al*., 2004; Collins *et al*., 2009; Newbury, 2008) have also aided in improvements in X-ray analysis at low voltages. Additional benefit of lower kV is the reduction in X-ray absorption; this suggests that the quantitative analysis at lower voltages should be more accurate than at high kV for the same number of X-ray counts in the spectrum (Gauvin, 2006).

The low voltage X-ray analysis, however, comes with some caveats. Some elements are difficult to detect at low voltages, and the user should be careful in the selection of the accelerating voltage. For instance, if the material of interest is silicon, the user requires at least 3.5 kV accelerating voltage to get significant counts for X-ray analysis (Si K line is at 1.74 kV). Peak overlap is also problematic at lower voltages, where multiple elements have K, L and M X-ray lines. The user should also be careful about specimen contamination and hydrocarbon buildup on the specimen surface during low voltage analysis, which can have a detrimental effect on the counting statistics and therefore eventual quantitative analysis.

1.7 TEM/STEM IMAGING AND ANALYSIS AT LOW VOLTAGES

The main driving force behind resurgence of low voltage transmission electron microscopy in the recent years is the potential to significantly reduce the knock-on beam damage and thus improve the ability to effectively observe and characterize at atomic scale new types of

nanomaterials. Another important advantage of low voltage TEM and STEM is enhanced contrast due to energy dependent scattering behavior.

The incorporation of aberration correctors, in particular the successful adoption of C_s correctors in TEM columns has allowed the increased resolution now possible at sub-Ångström levels. In the process of improving the resolution at high accelerating voltages, that is, above 200 kV, the C_s corrector has also enabled the improvement of resolution at lower energies (<120 keV). Low-voltage High-Resolution Electron Microscopy (LVHREM) has several advantages: increased cross-sections for inelastic and elastic scattering and hence higher contrast efficiency from each atom, as well as reduced radiation knock-on damage to samples insensitive to other damage mechanisms, which includes most metals, semiconductors and other solid state materials.

Historically, the use of higher TEM voltages was favored since they reduce the spherical and chromatic aberration effects; however, the development of spherical aberration correctors has allowed atomic resolution at 60 kV (Krivanek *et al*., 2008).

Although the TEM samples must be significantly thinner for low kV observation, the improvement in contrast for inorganic materials, organics, biological samples and especially nanobiological samples in low-voltage TEM while retaining atomic resolution cannot be understated. Damage mechanisms for biological samples are complicated and very structure dependent.

Lower beam energy is also important for obtaining the highest possible energy stability for spectroscopy applications. At 40 kV using an electron monochromator a beam with energy distribution at a full width at half maximum of less than 50 meV can be obtained. By reducing the voltage of the TEM, there are distinct gains in using electron energy-loss spectroscopy to determine band gaps and the dielectric properties with nanometer spatial resolution: the relativistic losses are reduced and delocalization of the energy-loss signal is reduced with the energy of the incident probe. Since C_c is both expensive and difficult to correct, the resolution improvement by using a monochromator is an effective option for materials applications. Details of low voltage TEM will be described in a Chapter 5 in this volume. Applications of low voltage STEM and EDS will be presented in Chapters 6 and 7.

1.8 CONCLUSION

There are significant advantages to low voltage operation across the different electron optical platforms. In the case of SEM, the significant reduction in interaction volume at lower kVs allows the user to obtain

surface sensitive information that would be impossible to observe at high kV. Low voltage operation also promotes imaging on non-conductive specimens without the need for conductive coating, and imaging of beam sensitive materials without inducing extensive radiation damage. Furthermore, changes in the secondary and backscatter yields open avenues for new and previously untapped contrast mechanisms. There are very distinct differences between the important considerations for low voltage SEM imaging as compared to TEM and STEM imaging and these will be detailed in the later chapters of this volume.

REFERENCES

D.C. Bell, C.J. Russo, and D.V. Kolmykov, 40 keV atomic resolution TEM, *Ultramicroscopy*, **114**, 31–37 (2012).

G.A. Botton, S. Lazar, and C. Dwyer, Elemental mapping at the atomic scale using low accelerating voltages, *Ultramicroscopy*, **110**, 926–934 (2010).

E.D. Boyes, On low voltage scanning electron microscopy and chemical microanalysis, *Microsc. Microanal.*, **6**, 307–316 (2000).

C. Bouchard and J.D. Carette, The surface potential barrier in secondary emission from semiconductors, *Surf. Sci.*, **100**, 241–250 (1980).

R. Browning, T.Z. Li, B. Chui, *et al.*, *Low-energy electron/atom elastic scattering cross sections* from 0.1–30 keV, *Scanning*, **17**, 250 (1995).

J. Cazaux, Charging in scanning electron microscopy "from inside and outside", *Scanning*, **26**, 181–203 (2004).

J. Cazaux, On some contrast reversals in SEM: application to metal/insulator systems, *Ultramicroscopy*, **108**, 1645–1652 (2008).

C. Colliex and C. Mory, Quantitative aspects of scanning transmission electron miscoscopy, in *Quantitative Electron Microscopy*, J.N. Chapman and A.J. Craven (eds.), Scottish Universities Summer School in Physics, Edinburgh, 149–216 (1984).

C.L. Collins, J. Holland, S.R. Burgess, and N. Rowlands, X-Max Large Area SDD Detectors - Creating a Real Impact on Nano-Science, *Microsc. Microanal.*, **15**, 172–173 (2009).

V.E. Cosslett, Probe size and probe current in the STEM, *Optic*, **36**, 85–92 (1972).

A.J. Dekker, Secondary electron emission, in *Solid State Physics*, F. Seitz and D. Turnbull (eds.), Academic Press, Inc., 251–311 (1958).

Z. Czyzewski, D.O. MacCallum, A. Romig, and D.C. Joy, Calculations of Mott scattering cross-section, *J. Appl. Phys.*, **68**, 3066 (1990).

E.H. Darlington, Backscattering of 10–100 keV electrons from thick targets, *J. Phys. D*, **8**, 85–93 (1975).

E.H. Darlington and V.E. Cosslett, Backscattering of 0.5–10 keV electrons from solid targets, *J. Phys. D*, **5**, 1969–1981 (1972).

H. Drescher, L. Reimer, and H. Seidel, Backscattering and secondary electron emission of 10–100 keV electrons and correlations to scanning electron microscopy, *Z. Ang. Physic*, **29**, 331–338 (1970).

D. Drouin, A.R. Couture, D. Joly, *et al*., CASINO V2.42—A fast and easy-to-use modeling tool for scanning electron microscopy and microanalysis users, *Scanning*, **29**, 92–101 (2007).
R.F. Egerton, *Electron Energy Loss Spectroscopy in the Electron Microscope*, 3rd edn, Plenum Press, New York, (2011).
R. Gauvin and D. Drouin, A formula to compute total elastic Mott cross-sections, *Scanning*, **15** (3), 140–150 (1993).
R. Gauvin, K. Robertson, P. Horny, *et al*., Materials characterization using high-resolution scanning electron microscopy and X-ray microanalysis, *JOM*, **58** (3), 20–25 (2006).
J. Goldstein, D.E. Newbury, D.C. Joy, *et al*., *Scanning Electron Microscopy and X-Ray Microanalysis*, 3rd edn, Springer, New York, (2003).
M. Haider, G. Braunshausen, and E. Schwan, Correction of the spherical-aberration of a 200-kV TEM by means of a hexapole-corrector, *Optik*, **99**, 167 (1995).
P.W. Hawkes and E. Kasper, *Principles of Electron Optics*, vol. **1**, Academic Press, London (1985).
L.W. Hobbs, *Introduction to Analytical Electron Microscopy*, p. 437, J.J. Hren, J.I. Goldstein, and D.C. Joy (eds), Scanning Microscopy International, Chicago (1979).
L.W. Hobbs and M.R. Pascucci, Radiolysis and defect structure in electron-irradiated α-quartz, *J. Phys. Colloques*, **41**, 237 (1980).
P. Hovington, D. Drouin, R. Gauvin, *et al*., CASINO: A new Monte Carlo code in C language for electron beam interactions—Part III: Stopping power at low energies, *Scanning*, **19**, 29–35 (1997).
D. Joy, A database on electron-solid interactions, *Scanning*, **17**, 270–275 (1995).
D. Joy, Aberration-Corrected SEM, in *Biological Low-Voltage Scanning Electron Microscopy*, H. Schatten and J.B. Pawley (eds), Springer, Heidelberg (2008).
D.C. Joy and C.S. Joy, Low Voltage Scanning Electron Microscopy, *Micron*, **27**, 247–263 (1996).
E.A. Kenik, D.C. Joy and D. Redfern, Microcalorimeter detectors and low voltage SEM microanalysis, *Microchim. Acta*, **145**, 81–85 (2004).
M. Knoll, Aufladepotentiel und Sekundäremission elektronenbestrahlter Körper, *Z. tech. Phys*., **16**, 467–475 (1935).
M. Kotera, K. Murata, and K. Nagami, Monte Carlo simulation of 1–10 keV electron scattering in a gold target, *J. Appl. Phys*., **52**, 997–1003 (1981a).
M. Kotera, K. Murata, and K. Nagami, Monte Carlo simulation of 1–10 keV electron scattering in an aluminum target, *J. Appl. Phys*., **52**, 7403–7408 (1981b).
O.L. Krivanek, N. Dellby, R.J. Keyse, *et al*., Aberration-corrected STEM and EELS, in *Advances in Imaging and Electron Physics*, P.W. Hawkes (ed.), Elsevier, Amsterdam (2008).
F. Lenz, Zur Streuung mittelschneller Elektronen in kleinste Winkel, *Z. Naturforsch*., **9A**, 185–204 (1954).
H. Mahl, Supermicroscopic determination of the orientation of single aluminium crystals (in German), *Metallwirtschaft*, **19**, 1082–1085 (1940).
D. McMullan, *Investigations relating to the design of electron microscopes*, Ph.D. dissertation, University of Cambridge, (1952).
D. McMullan, A history of the scanning electron microscope, 1928–1965, *Adv. Imaging Electron Phys*., **133**, 523–545 (2004).

N.F. Mott, The polarisation of electrons by double scattering, *Proc. R. Soc. London A*, **135**, 429 (1932).
N.F. Mott and H.S.W. Massey, *The Theory of Atomic Collisions*, Clarendon Press, Oxford, (1949).
D.A. Muller, L. Fitting-Kourkoutis, M. Murfitt, *et al*., Atomic-scale chemical imaging of composition and bonding by aberration-corrected microscopy, *Science*, **319**, 1073 (2008).
D.E. Newbury, Developments in instrumentation for microanalysis in low-voltage scanning electron microscopy, in *Biological Low-Voltage Scanning Electron Microscopy*, H. Schatten and J.B. Pawley (eds), Springer, Heidelberg (2008).
M.R. Pascucci, J.L. Hutchison, and L.W. Hobbs, The metamict transformation in alpha-quartz, *Radiat. Eff*., **74**, 219 (1983).
L. Reimer, *Image Formation in Low-Voltage Scanning Electron Microscopy*, *Vol. TT 12*, SPIE, Bellingham, WA (1993).
L. Reimer and H. Kohl, *Transmission Electron Microscopy*, *Physics of Image Formation and Microanalysis*, Springer, Berlin (2008).
L. Reimer and C. Tollkamp, Measuring the backscattering coefficient and secondary electron yield inside a SEM, *Scanning*, **3**, 35–39 (1980).
H. Rose, *Geometrical Charged Particle Optics*, Springer, Berlin/Heidelberg (2009).
N. Rowlands, N. Erdman and V. Robertson, Characterization of nanoscale structures using a combination of an ultra-high resolution field emission SEM and large area silicon drift detector, *Microsc. Microanal*., **15**, 548–549 (2009).
E. Ruska, The electron microscopic imaging of surfaces of surfaces irradiated with electrons (in German), *Z. Phys*., **83**, 492–497 (1933).
E. Rutherford, Elastic cross section, *Phil. Mag*., **21**, 669–680 (1911).
R.F.M. Thornley, *New applications of the electron microscope*, Ph.D. dissertation, University of Cambridge, (1960).
R. Schmid, K.H. Gaukler, and H. Seiler, Measurement of elastically reflected electrons ($E \leq 2.5$ keV) for imaging of surfaces in a simple ultrahigh vacuum SEM, *Scanning Electron Microscopy 1983/II*, SEM Inc., AMF O'Hare, 501–509 (1983).
H. Seiler, Secondary electron emission in scanning electron microscope, *J. Appl. Phys*., **54**, R1–R18 (1983).
O. Ugurlu, J. Haus, A.A. Gunawan, *et al*., Radiolysis to knock-on damage transition in zeolites under electron beam irradiation, *Phys. Rev. B*, **83**, 113408 (2011).
M. von Ardenne, *Improvements in electron microscopes*, British Patent No. 511204 (1937).
M. von Ardenne, The scanning electron microscope. Theoretical fundamentals (in German), *Z. Phys*., **109**, 553–572 (1938).
M. von Ardenne, On the history of scanning electron microscopy, the electron microprobe, and early contributions to transmission electron microscopy, in "The beginnings of electron microscopy" (P.W. Hawkes, ed.), *Adv. Electonics Electr. Phys*., **Suppl. 16**, 1–21 (1985).
O.C. Wells, *The construction of a scanning electron microscope and its application to the study of fibres*. PhD Dissertation, Cambridge University (1957).
V.A. Zworykin, J. Hillier, and R.L. Snyder, A scanning electron microscope, *ASTM Bull*., **117**, 15–23 (1942).